scientific reports



OPEN

The origin and influence of noncavity modes in a micropillar Bragg microcavity

Matthew Jordan¹, Wolfgang Langbein ³ & Anthony J. Bennett ¹,2 □

Controlling the photonic environment of emitters is essential to the design of classical and quantum light sources. We study the case of a dipole-like emitter in a cylindrical pillar etched into a planar Bragg microcavity, which is a common design of quantum-dot single photon source. In addition to the well-known cavity modes created by the high-reflectivity of the Bragg mirrors at small in-plane wavevectors, we show the presence of broad spectral features that play a key role in controlling photon collection efficiency and Purcell enhancement. These 'non-cavity' modes are insensitive to the periodic index modulation of the Bragg reflectors, but arise from the cylindrical pillar geometry, as we show by comparison with simulations of uniform pillars, which reproduce the non-cavity modes. This approach provides a tool for understanding and modelling these often-disregarded decay channels as a function of source height, cavity dimensions and surface layers.

The emission dynamics and efficiency of point sources in cavities is of both fundamental interest and critical for the development of photon sources for quantum technology. Cavity designs based around periodic variations in dielectric can result in high-quality factor modes, such as in photonic crystals¹⁻³, Bragg-cavities⁴⁻⁹, and 'bullseye' circular gratings¹⁰⁻¹². To achieve maximum Purcell factor and efficiency, emitters in these structures are generally assumed to couple maximally to the localised cavity modes.

The semiconductor quantum dot (QD) micropillar cavity is a popular choice of solid state device for the generation of indistinguishable single photons^{13–15}, as required by a wide range of quantum applications^{16–19}, courtesy of its ease of fabrication and high performance. These structures consist of a cavity spacer layer sandwiched between two distributed Bragg reflectors (DBRs). Reducing the lateral dimensions results in discrete optical cavity modes, localized between the mirrors, the lowest energy of which (HE₁₁) couples well to a far field collection optic such as a fibre or a lens^{20,21}. Many studies have focused on maximizing the quality factor, Qof HE₁₁ to obtain the highest photon collection efficiency^{22,23} but this places a tight constraint on the detuning between the emitter's transition(s) and the mode, which can result in a low yield of efficient devices. Simulations have shown that even in an optimally coupled QD-cavity device the efficiency and Purcell factor display a periodic behaviour as a function of diameter^{24,25}. This is a result of the interplay between coupling to the HE_{11} and lower-Q leaky "non-cavity" modes which radiate over a larger solid angle. It has recently been established that lower quality factor (Q < 1000) microcavities can also offer very high efficiency^{24,26}, still host dots capable of indistinguishable photon emission 15 , and offer a more favourable tolerance to detuning. However, these lower- Qdevices are more strongly affected by the non-cavity modes, which justifies a detailed study of their origin and behaviour. These non-cavity micropillar modes are spectrally broad and overlap, making them difficult to extract from such simulations, but as they provide alternative decay channels for the source, understanding them is essential to maximize efficiency²⁷.

In the weak-coupling regime the emission into a single mode is parameterized by the Purcell factor $F_{\rm P}$, defined as the ratio of total decay rate in the cavity - into the localized cavity mode $\Gamma_{\rm C}$ and the other non-cavity modes $\Gamma_{\rm L}^{28}$ - relative to the decay rate in a homogenous medium $\Gamma_{\rm 0}$. In the case where $\Gamma_{\rm C} >> \Gamma_{\rm L}$ the Purcell factor of an emitter of free-space wavelength λ can be approximated with the mode volume V, quality factor Q, and effective refractive index $n_{\rm eff}^{29}$:

$$F_{\rm P} = \frac{\Gamma_{\rm C} + \Gamma_{\rm L}}{\Gamma_{\rm 0}} \approx \frac{3Q\lambda^3}{4\pi^2 V n_{\rm eff}^3} \tag{1}$$

¹School of Engineering, Cardiff University, Queen's Buildings, The Parade, Cardiff CF24 3AA, UK. ²Translational Research Hub, Maindy Road, Cardiff CF24 4HQ, UK. ³School of Physics and Astronomy, Cardiff University, Queen's Buildings, The Parade, Cardiff CF24 3AA, UK. [™]email: BennettA19@cardiff.ac.uk

Whereas the cavity modes are localized between the mirrors and can be simulated in finite-difference time-domain (FDTD) or finite element method (FEM) simulations using established numerical techniques, the leaky channels are often neglected from interpretation of the results. Although it is commonly assumed that $\Gamma_{\rm L} \approx \Gamma_0$, this is an over-simplification²⁵, which neglects the influence of the non-cavity modes on the local photon density of states³⁰.

Here we study the relationship between the non-cavity modes and the gross shape of the adjacent semiconductor/air interfaces, by comparing simulations of cavities and identically shaped devices with a uniform refractive index. Simulations performed as a function of pillar diameter, source position and the position of the top surface are compared for cavities and uniform pillars. This work offers a method of modelling non-cavity mode behaviour, providing insights into their origin and potential optimization in future solid-state quantum light sources.

Resonant behaviour of non-cavity modes in a Bragg micropillar as a function of diameter

For all simulation results shown we use ANSYS Lumerical FDTD. We consider here a cylindrical micropillar consisting of a 267.9 nm 1λ GaAs spacer layer between DBRs of λ /4 alternating Al $_{0.95}$ Ga $_{0.05}$ As (78.9 nm) and GaAs (67.0 nm) layers, 7 above and 26 pairs below, on a planar GaAs substrate. This semiconductor stack is etched into cylindrical micropillars with vertical sidewalls running down to the substrate surface, with diameters between 1.5 and 4.0 µm. Material properties are modelled using the wavelength-dependent refractive index data for GaAs (3.55 at 940 nm) and Al $_{0.95}$ Ga $_{0.05}$ As (2.94 at 940 nm). The refractive indices of the materials include dispersion and neglect absorption Capacitae (2.94 at 940 nm). The refractive indices of the materials include dispersion and neglect absorption of 20 emission is modelled as an electric dipole source at x=y=z=0, in the geometric centre of the spacer layer, oriented along the x-axis. z is the symmetry axis of the cavity. The dipole is driven with a Gaussian pulse of 5.6 fs full width at half maximum (FWHM), covering a spectral range from 840 nm to 1070 nm. The simulation volume has x and y dimensions of 5.5 µm and a z dimension of 10 µm centred on the dipole at the centre of the spacer, with perfectly matched layers at the simulation boundaries. Each surface of the simulation volume has a planar frequency-domain field monitor to record the local electric and magnetic fields and the Poynting vector, allowing the transmission spectrum to be calculated, through the surface of a cuboid around the pillar. Additionally, two planar frequency-domain monitors form cross-sections through the structure on the x=0 and y=0 planes. A schematic of the simulation environment, including these monitors, is shown in Fig. 1a.

The FDTD simulation outputs the spatial and spectral sum of all fields. Unlike complementary analytical simulation methods, such as the Fourier Modal Method 32,33 or Resonant State Expansion technique 30 , FDTD does not explicitly separate different classes of mode. Thus, we define "cavity" modes as those arising from the strong reflection of the Bragg mirrors, which are spatially localized between said mirrors and have quality factors consistent with those mirrors' high reflectivity. All other spectral features are hereafter referred to as non-cavity modes. Figure 1b shows the normalised far-field angular intensity distribution of the fundamental HE $_{11}$ cavity mode in a 2.00 μ m diameter micropillar, as calculated from the electric field distribution at the top simulation surface monitor T_{+z} . Spectrally-resolved power through this monitor (Fig. 1c) and the complete surface formed by the six surrounding monitors (Fig. 1d), reveals a Lorentzian feature with a quality factor of \sim 600, consistent with analytical models of the HE $_{11}$ mode 34 . In addition to this, a broadband background of emission is observed, which dramatically modifies the spectrum at this micropillar diameter, indicating the importance of understanding these non-cavity modes.

It is possible to extract the Purcell factor, cavity mode emission, and non-cavity mode emission at the HE $_{11}$ resonance wavelength from the total emission spectrum of the micropillar. First, the Purcell factor ($F_{\rm P}$) will be equal to the total emission power normalised by the total power injected via the dipole at the cavity mode wavelength, which can be calculated as a sum of transmitted power through the closed surface of monitors. The proportion of emission via the cavity mode ($\Gamma_{\rm C}$) on resonance can then be determined using a least-squares curve fit consisting of a Lorentzian cavity mode superimposed on a broadband Lorentzian background of non-cavity modes ($\Gamma_{\rm L}$), as demonstrated in Fig. 1d. This serves as a fair approximation in this case, but it should be noted that there may generally be interference between modes, as they emit into non-orthogonal outgoing channels. The behaviour as a function of pillar diameter is plotted in Fig. 1e. The spontaneous emission (SE) β is plotted in Fig. 1f.

 $\Gamma_{\rm C}$ decreases as a function of diameter with an inverse-square relationship due to the increased mode volume (see Eq. (1))³⁵. Interestingly, $\Gamma_{\rm L}$ varies periodically with diameter, having a period of 0.278 µm which is close to $\lambda/n_{\rm GaAs}$, suggesting some resonant behaviour with the pillar sidewalls. $\Gamma_{\rm L}$ takes values ranging from 0.35 to 2.24 $\Gamma_{\rm O}$, showing a coupling to non-cavity modes ranging from suppression to enhancement, which is modulating $F_{\rm P}$. This also results in a periodic behaviour in β , which also decreases gradually with diameter due to the reduction in $\Gamma_{\rm C}$. Although direct comparison of our results with previous literature is complicated by differences in design wavelength and number of repeats in the Bragg mirrors, other works have also reported periodic oscillations in $F_{\rm P}$ and β with diameter^{23,25,26} and shown it has an important influence on the achieving the highest efficiencies and indistinguishability.

Comparing uniform pillars with micropillar cavities

To gain insight into the behaviour of the non-resonant modes without the effect of the resonant cavity, we replace the structured refractive index of the micropillar with a uniform index. We used the wavelength-dependent refractive index data for GaAs and $Al_{0.95}Ga_{0.05}As$ to determine a mean index weighted for the relative volumes

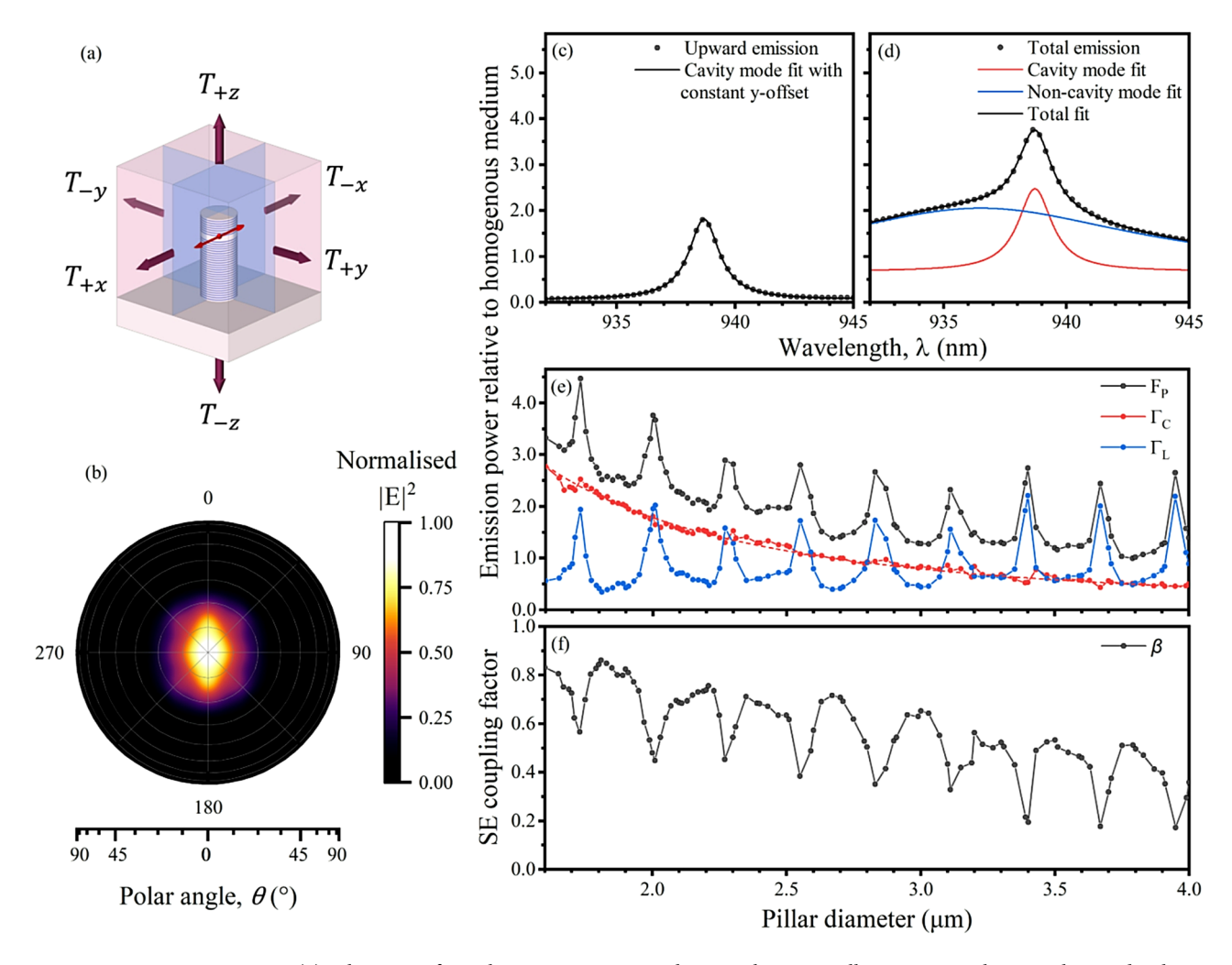


Fig. 1. (a) Schematic of simulation environment, showing the micropillar on GaAs substrate, electric dipole source (red), cross-sectional (blue) and simulation boundary surface (purple) frequency-domain plane monitors, the latter labelled according to the transmission component measured through the monitor in each direction. (b) Simulated normalised far-field intensity, $|\mathbf{E}|^2$, angular emission profile above a 2.00 µm diameter micropillar with 7 (26) upper (lower) DBR pairs. (c) Simulated emission power spectrum in the upward direction and (d) summed over all directions. Cavity and non-cavity modes fitted with Lorentzian curves. (e) Purcell factor $F_{\rm P}$, cavity mode emission $\Gamma_{\rm C}$, and non-cavity mode emission $\Gamma_{\rm L}$ and (f) spontaneous emission (SE) coupling factor β as a function of pillar diameter. All emissions are normalised to the source emission power in a homogenous medium. The cavity mode emission rate was fitted with an inverse-square relationship as a function of diameter (dashed).

of each material in the cavity (3.23 at 940 nm). This averaging of the refractive index results in the same optical path length along the pillar.

Keeping the position of the electric dipole source, the resulting Purcell factor F_P is given in Fig. 2 versus pillar diameter for both the Bragg cavity (a, b) and the uniform pillar (c, d). Panels (a, c) use only the emission transmitted through the top and bottom monitors, T_{+z} and T_{-z} , which we call vertical emission, while (b, d) show the total emission spectra, including side or "lateral" emission, determined from the emission through all surfaces of the enclosed volume.

Disregarding the HE_{11} and higher order cavity modes, visible as steep narrow streaks in (a, b) and marked with red arrows, which vanish in the absence of the periodic layers, notable similarities exist between the two simulations. In particular, periodic broad diagonal features are visible which red-shift with diameter. In the vertical emission (a, c), two broad diagonal features cross one another with different gradients, indicated with blue dashed lines, as a result of different numbers of repeats in the top and bottom mirrors and thus the dipole source not being vertically centred in the pillar. The periodicities of the lines are well-reproduced by the uniform pillar, as are their phases, suggesting the uniform pillar is providing a useful approximation of the non-cavity modes. Previous work studying pillars of much smaller diameter using the Fourier Modal Method attributes broad spectral features to Bloch modes in the Bragg mirrors 32,33 .

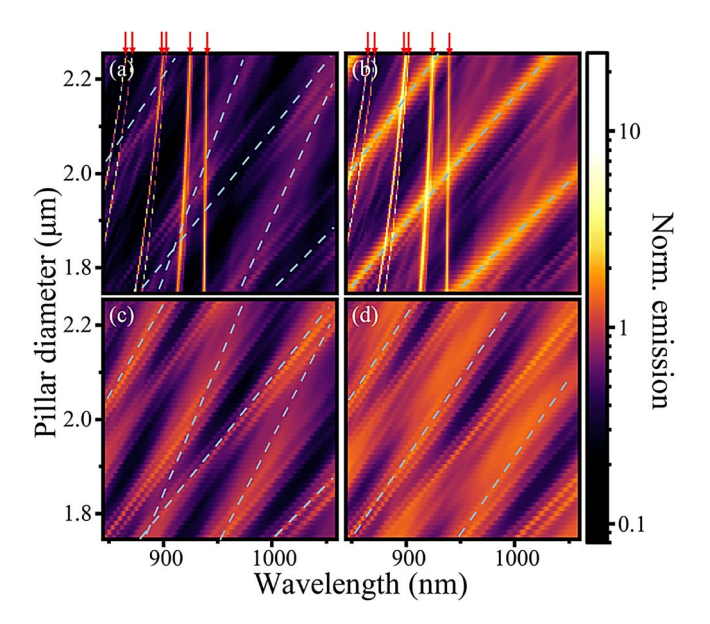


Fig. 2. Purcell factor for a source in the centre of the spacer layer, in a Bragg cavity (\mathbf{a},\mathbf{b}) or uniform (\mathbf{c},\mathbf{d}) pillar as a function of pillar diameter. In (\mathbf{a},\mathbf{c}) only the emission through the top and bottom monitors T_{+z} and T_{-z} are considered while in (\mathbf{b},\mathbf{d}) emission through all sides is considered. Red arrows indicate the positions of the cavity modes, whilst blue dashed lines highlight the gradients of some broad spectral features which appear in the cavity and the uniform pillar.

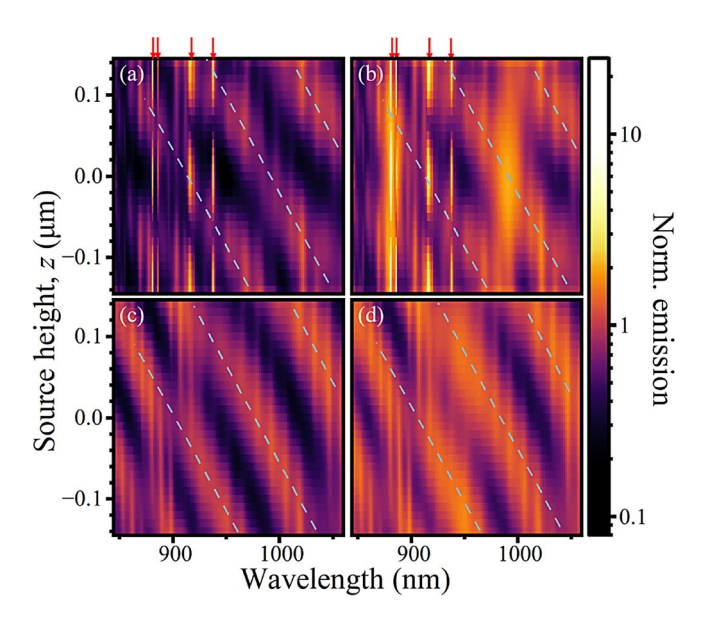


Fig. 3. Purcell factor for a source in a Bragg cavity (\mathbf{a},\mathbf{b}) or uniform (\mathbf{c},\mathbf{d}) pillar for a constant pillar diameter of 1.85 μ m, as function of the source height. In (\mathbf{a},\mathbf{c}) only the emission through the top and bottom monitors T_{+z} and T_{-z} are considered while in (\mathbf{b},\mathbf{d}) emission through all sides is considered. Red arrows indicate the positions of the cavity modes, whilst blue dashed lines highlight the gradients of some broad spectral features which appear in the cavity and the uniform pillar.

This insight is further explored by changing the dipole source's height z in pillars of 1.85 μ m diameter, as shown in Fig. 3. The source height is varied over the full extent of the 1 λ cavity spacer layer. In (a), the interaction between the source and cavity mode standing wave is apparent, having an anti-node in the centre and at the edges of the spacer. Beyond the sharp fundamental and higher order cavity modes, the broad features arising from the uniform pillar (c, d) display comparable broad features with the same periodicity and gradient to the non-cavity mode behaviour in (a, b). Non-cavity modes blue-shift with increasing z at similar rates in

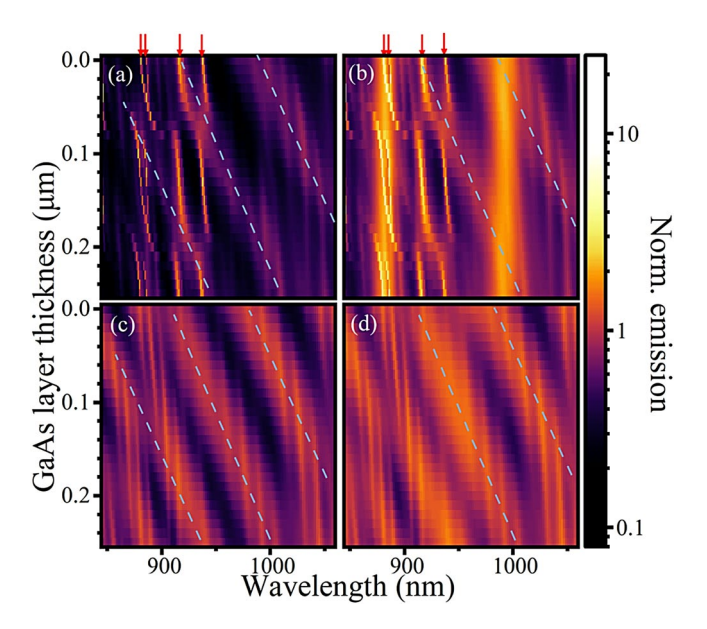


Fig. 4. Purcell factor for a source in the centre of the spacer layer, in a Bragg cavity (\mathbf{a},\mathbf{b}) or uniform (\mathbf{c},\mathbf{d}) pillar for a constant pillar diameter of 1.85 μ m, as function of an additional GaAs layer added to the top of the pillar. In (\mathbf{a},\mathbf{c}) only the emission through the top and bottom monitors T_{+z} and T_{-z} are considered while in (\mathbf{b},\mathbf{d}) emission through all sides is considered. Red arrows indicate the positions of the cavity modes, whilst blue dashed lines highlight the gradients of some broad spectral features which appear in the cavity and the uniform pillar.

both structures, and show similar periods, with a small offset in phase. This blueshift with dipole height is caused by the Bloch modes within the Bragg mirrors^{23,32}: decreasing distance to the top surface, which provides a strong reflection shifts the resonance condition. The bottom surface to the substrate instead has only a small index step and accordingly has a lower reflectivity. The standing waves forming are thus similar to open pipe oscillations, which would suggest a scaling of the non-cavity mode's wavelength, λ , as a function of the distance between the emitter and the top surface of the pillar, d, varying as:

$$\lambda \propto \frac{1}{\sqrt{\frac{b^2}{r^2} + \frac{a^2}{d^2}}} \tag{2}$$

Where r is the radius, and a and b are constants. Indeed, in both structures there are discrete bright resonances that pass-through nodes and antinodes as the dipole height is changed with a period greater than the wavelength, because we only see the z-component of the wavevector interact with the open-pipe modes along z.

Finally, the pillars were modified by adding a layer of GaAs with varying thicknesses to the top surface (Fig. 4). This modifies the phase of the back-reflection from the top GaAs/air interface for the cavity mode, decreasing the Q factor of the cavity mode due to the change from constructive to destructive interference at $\lambda/4$ thickness of about 70 nm and back to constructive at $\lambda/2$ thickness. For the non-cavity modes, adding the layer is increasing the distance between emitter and surface (d). The resulting broad spectral features display similar periodicity and shift with similar gradients in the two models, as indicated by the dashed lines included in Fig. 4. This may be expected because they arise from either reflections of the Bloch modes in the top Bragg mirror reflecting from the cavity top surface or from the refection of the same surface in the uniform pillar. The distance from the dipole to the GaAs substrate does not change. Evidently, the addition of this GaAs spacer has implications for the optimisation of the pillar diameter and photon collection strategy.

Field profiles of cavities and uniform pillars

Overall, the model which uses a uniform micropillar consisting of a material with the weighted mean of GaAs and $Al_{0.95}Ga_{0.05}As$ refractive indices provides a good approximation to the non-cavity modes of a low Q micropillar. The reason for this is elucidated by the cross-sectional electric field profiles in Fig. 5. Emission is mostly directed into the +z direction (a, b) due to the larger number of bottom Bragg pairs. However, when the source is moved to the HE_{11} node it couples only to the non-cavity modes resulting in a complex field pattern (Fig. 5c, d). Similarities are visible in the field patterns within the uniform pillar when the dipole is at the same height (e, f). This supports the idea that the non-cavity modes have a similar spatial distribution to the uniform pillar which is to be expected when one considers the similarities between the Bloch modes in the Bragg mirrors 32,33 and the standing waves in the uniform pillar.

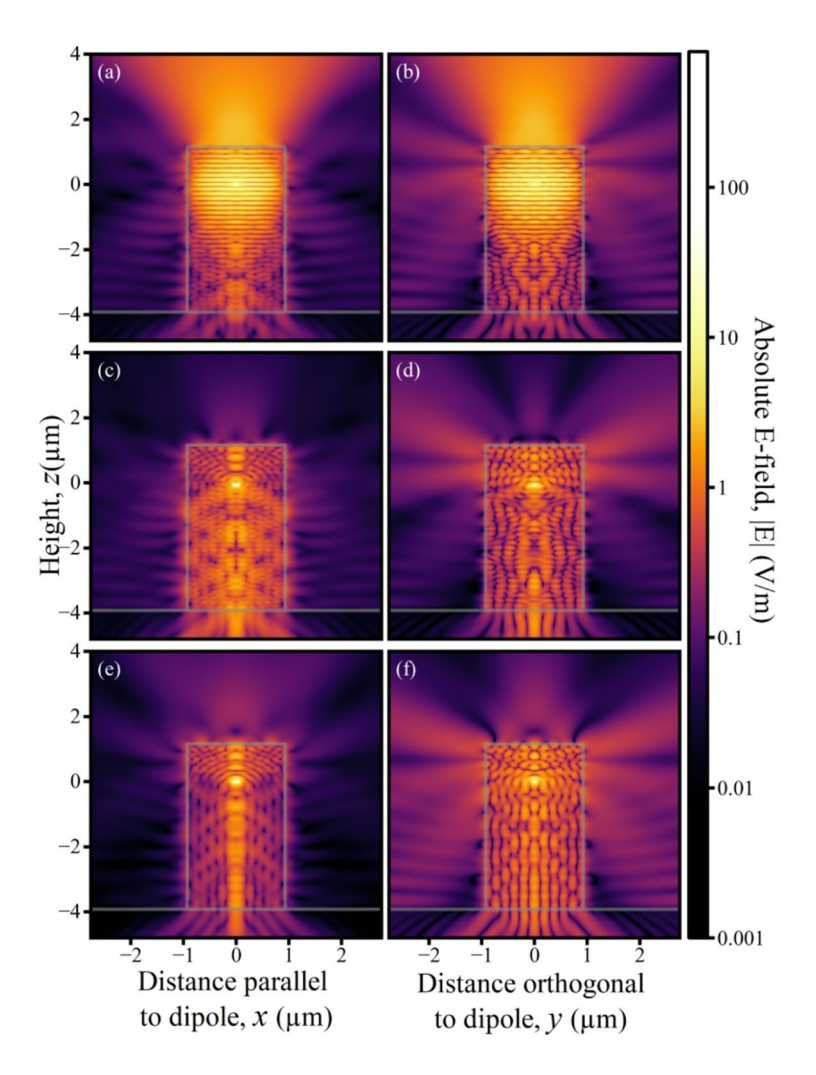


Fig. 5. Absolute electric field |E| cross-sectional profiles for 1.85 μm micropillars (grey outline) at the HE₁₁ mode wavelength for a cavity pillar excited by a dipole at the cavity mode anti-node (z=0 μm) in the centre of the spacer layer, in (a) on the y=0 plane (x-z), parallel to the dipole and in (b) on the x=0 plane (y-z), perpendicular to it. (c,d) as (a,b), but for a dipole at the lower cavity mode node (z=-0.067 μm). (e,f) as (a,b), but for a uniform micropillar.

Notably, we see in (e) a beam in the centre of the pillar, with is dominated by modes with a radial quantum number of 5. (f) shows a plane of strong dipole emission, orthogonal to the dipole. One can also note the directional emission towards the bottom, due to the reflection on the top surface.

Conclusion

In conclusion, the non-cavity mode behaviour is reproduced by the uniform pillar with a refractive index taken to the be the weighted mean of the cavity indices. These non-cavity modes are dependent on the diameter of the micropillar, red-shifting much faster than cavity modes within the simulated wavelength range. Simulations where the emitter height is varied, and where an additional layer is introduced in both the cavity and the uniform pillar, confirm that the "non-cavity" modes are determined by the gross shape of the micropillar. Images of the field intensity in the uniform pillar also show similarities to the field intensity of an emitter at the field node in a cavity.

This insight can offer additional tuning knobs to intuitively design optimum cavities, where the aim is often to minimise the effect of the non-cavity modes. In future, uniform-index approximations of the pillar structure and analytical solutions for the non-cavity mode spectrum, such as that presented in Eq. (2), can narrow the parameter space required for exact FDTD optimisations. These insights are particularly relevant to low- Q micropillars where the non-cavity modes have a greater influence on the performance metrics but are also relevant to efforts to engineer the most efficient high- Q cavities.

Data availability

The datasets generated in this study are available at the https://doi.org/10.17035/cardiff.30238336.

Received: 6 June 2025; Accepted: 25 September 2025

Published online: 31 October 2025

References

- 1. Yoshie, T. et al. Vacuum Rabi splitting with a single quantum Dot in a photonic crystal nanocavity. Nature 432, 200-203 (2004).
- Lodahl, P. et al. Controlling the dynamics of spontaneous emission from quantum Dots by photonic crystals. Nature 430, 654–657 (2004).
- 3. Liu, F. et al. High Purcell factor generation of indistinguishable on-chip single photons. Nat. Nanotechnol. 13, 835-840 (2018).
- 4. Gérard, J. M. et al. Enhanced spontaneous emission by quantum boxes in a monolithic optical microcavity. *Phys. Rev. Lett.* 81, 1110 (1998).
- 5. Ding, X. et al. On-demand single photons with high extraction efficiency and near-unity indistinguishability from a resonantly driven quantum Dot in a micropillar. *Phys. Rev. Lett.* **116**, 020401. https://doi.org/10.1103/PhysRevLett.116.020401 (2016).
- 6. Somaschi, N. et al. Near-optimal single-photon sources in the solid state. Nat. Photonics. 10, 340-345 (2016).
- 7. Unsleber, S. et al. Highly indistinguishable on-demand resonance fluorescence photons from a deterministic quantum Dot micropillar device with 74% extraction efficiency. Opt. Express. 24, 8539–8546 (2016).
- 8. Bennett, A. J. et al. Cavity-enhanced coherent light scattering from a quantum Dot. Sci. Adv. 2, e1501256. https://doi.org/10.1126/sciadv.1501256 (2016).
- 9. Reitzenstein, S. et al. AlAs/ GaAs micropillar cavities with quality factors exceeding 150.000. Appl. Phys. Lett. 90 (2007).
- 10. Davanco, M., Rakher, M. T., Schuh, D., Badolato, A. & Srinivasan, K. A circular dielectric grating for vertical extraction of single quantum Dot emission. *Appl. Phys. Lett.* **99** (2011).
- 11. Barbiero, A. et al. Design study for an efficient semiconductor quantum light source operating in the Telecom C-band based on an electrically-driven circular Bragg grating. Opt. Express. 30, 10919–10928 (2022).
- 12. Hekmati, R. et al. Bullseye dielectric cavities for photon collection from a surface-mounted quantum-light-emitter. Sci. Rep. 13, 5316 (2023).
- 13. Vahala, K. J. Optical microcavities. Nature 424, 839-846 (2003).
- Gerard, J. et al. Quantum boxes as active probes for photonic microstructures: the pillar microcavity case. Appl. Phys. Lett. 69, 449–451 (1996).
- 15. Androvitsaneas, P. et al. Direct-write projection lithography of quantum Dot micropillar single photon sources. *Appl. Phys. Lett.* **123**, 094001 (2023).
- 16. Magnitskii, S. et al. Metrology of single photons for quantum information technologies. Meas. Tech. 60, 235-241 (2017).
- 17. Kołodyński, J. et al. Device-independent quantum key distribution with single-photon sources. Quantum 4, 260 (2020).
- 18. Rudolph, T. Why I am optimistic about the silicon-photonic route to quantum computing. APL Photonics. 2, 030901 (2017).
- 19. Raussendorf, R. & Harrington, J. Fault-tolerant quantum computation with high threshold in two dimensions. *Phys. Rev. Lett.* **98**, 190504 (2007).
- 20. Reitzenstein, S. & Forchel, A. Quantum Dot micropillars. J. Phys. D. 43, 033001 (2010).
- 21. Connor, F. R. Wave Transmission (Edward Arnold, 1972).
- 22. Lermer, M. et al. Bloch-wave engineering of quantum Dot micropillars for cavity quantum electrodynamics experiments. *Phys. Rev. Lett.* **108**, 057402 (2012).
- 23. Wang, B. Y., Denning, E. V., Gür, U. M., Lu, C. Y. & Gregersen, N. Micropillar single-photon source design for simultaneous near-unity efficiency and indistinguishability. *Phys. Rev. B.* 102, 125301 (2020).
- Ginés, L. et al. High extraction efficiency source of photon pairs based on a quantum Dot embedded in a broadband micropillar cavity. Phys. Rev. Lett. 129, 033601 (2022).
- Jordan, M. et al. Probing Purcell enhancement and photon collection efficiency of InAs quantum Dots at nodes of the cavity electric field. Phys. Rev. Res. 6, L022004 (2024).
- 26. Dlaka, D. et al. Design principles for >90% efficiency and >99% indistinguishability broadband quantum Dot cavities. *New J. Phys.* **26**, 093022 (2024).
- Munsch, M. et al. Continuous-wave versus time-resolved measurements of Purcell factors for quantum Dots in semiconductor microcavities. Phys. Rev. B. 80, 115312 (2009).
- 28. Fox, A. M. Quantum Optics: an Introduction Vol. 15 (Oxford University Press, 2006).
- 29. Purcell, E. Spontaneous emission probabilities at radio frequencies. Phys. Rev. 69, 681-681 (1946).
- 30. Muljarov, E. A. & Langbein, W. Exact mode volume and Purcell factor of open optical systems. Phys. Rev. B. 94, 235438 (2016).
- 31. Palik, E. D. Handbook of Optical Constants of Solids Vol. 3 (Academic, 1998).
- 32. Lalanne, P., Hugonin, J. P. & Gérard, J. M. Electromagnetic study of the quality factor of pillar microcavities in the small diameter limit. *Appl. Phys. Lett.* **84**, 4726–4728 (2004).
- 33. Lecamp, G., Lalanne, P., Hugonin, J. P. & Gérard, J. M. Energy transfer through laterally confined Bragg mirrors and its impact on pillar microcavities. *IEE J. Quantum Electron.* 41, 1323–1329 (2005).
- 34. Schubert, E. F. Light-Emitting Diodes (E. Fred Schubert, 2018).
- 35. Khitrova, G., Gibbs, H., Kira, M., Koch, S. W. & Scherer, A. Vacuum Rabi splitting in semiconductors. Nat. Phys. 2, 81-90 (2006).

Author contributions

MJ: Conceptualization, Investigation, Data Curation, Writing—Original Draft, Writing—Review & Editing. WWL: Conceptualization, Writing—Review & Editing, Supervision AJB: Conceptualization, Writing—Review & Editing, Supervision, Project administration, Funding acquisition.

Funding

We acknowledge financial support from EPSRC Grant No. EP/T001062/1, EP/Z53318X/1 and EP/T017813/1.

Declarations

Competing interests

The authors declare no competing interests.

Additional information

Correspondence and requests for materials should be addressed to A.J.B.

Reprints and permissions information is available at www.nature.com/reprints.

Publisher's note Springer Nature remains neutral with regard to jurisdictional claims in published maps and institutional affiliations.

Open Access This article is licensed under a Creative Commons Attribution 4.0 International License, which permits use, sharing, adaptation, distribution and reproduction in any medium or format, as long as you give appropriate credit to the original author(s) and the source, provide a link to the Creative Commons licence, and indicate if changes were made. The images or other third party material in this article are included in the article's Creative Commons licence, unless indicated otherwise in a credit line to the material. If material is not included in the article's Creative Commons licence and your intended use is not permitted by statutory regulation or exceeds the permitted use, you will need to obtain permission directly from the copyright holder. To view a copy of this licence, visit https://creativecommons.org/licenses/by/4.0/.

© The Author(s) 2025